Polarization dynamics of a vector cavity soliton in a birefringent fiber resonator

Maitrayee Saha,[1,*] Samudra Roy,[1,2,†] and Shailendra K. Varshney[3,‡]

[1]*Department of Physics, Indian Institute of Technology Kharagpur, Kharagpur-721302, India*

[2]*Centre of Theoretical Studies, Indian Institute of Technology Kharagpur, Kharagpur-721302, India*

[3]*Department of Electronics and Electrical Communication Engineering, Indian Institute of Technology Kharagpur, Kharagpur-721302, India*

(Received 16 December 2019; accepted 2 March 2020; published 17 March 2020)

We investigate theoretically the polarization dynamics of vector cavity solitons in a birefringent fiber resonator exhibiting net anomalous dispersion. The well-known Lugiato-Lefever equation is adopted to capture the intracavity field dynamics when two orthogonal modes are coupled via nonlinear cross-phase modulation. Numerical simulations reveal the coexistence of different nonlinear states, such as cavity solitons (CSs) with a modulation instability pattern, two identical CSs, or a nonidentical pair of CSs depending on the external parameters. We distinguish three different types of coexisting CSs based on their polarization properties. Stokes parameters and Jones vector analysis are employed to extract the spatial energy flux distribution and the complex electric field associated with each polarization mode, respectively. We observe that the group-velocity mismatch affects the individual CS dynamics which has direct consequences of their polarization states. Our detailed findings with the polarization properties of CSs will enrich the understanding of dissipative vector CS dynamics in a passive birefringent fiber resonator.

DOI: 10.1103/PhysRevA.101.033826

I. INTRODUCTION

Cavity solitons (CSs) are temporally localized short optical pulses in a continuous-wave (cw) background. They belong to the dissipative soliton family that exists inside a passive Kerr cavity pumped by a coherent driving field. The existence of CSs was predicted theoretically in Ref. [1] and observed experimentally in a single-mode fiber resonator [2]. Since then CSs have gained considerable attention in other platforms such as microcavities which include ring resonators [3–5] and whispering gallery mode resonators [6,7]. A significant amount of research has been dedicated to understanding their origin, fundamental characteristics, and dynamics in the temporal domain [8–10] as well as their spectral signature in the form of a frequency comb [11–15]. It is a well-known fact that, apart from the trivial balance between the Kerr nonlinearity and dispersion in a passive dissipative system, an optical pulse can maintain its shape only when the total loss is compensated by an external cw pump source. The intracavity field dynamics in such a passive dissipative system can be characterized effectively with the Lugiato-Lefever equation (LLE) [16–18]. Recent trends show an interest in complex field evolution when different modes are coupled and are simultaneously excited [19–25]. In a microresonator system, mode coupling can occur in several ways, such as between clockwise (CW) and counterclockwise (CCW) modes [19,20], guided mode coupling near avoided mode crossings [21,22], and coupling between two orthogonally polarized modes in a microresonator [23] or in a birefringent fiber loop resonator [24,25]. It has been observed that multiple CSs can simultaneously exist without affecting each other and can be individually manipulated [26,27]. In particular, researchers have used dual pumping or a polychromatic driving field which excites different mode families of the resonator system, so that CSs with different polarization can coexist [28,29]. Recently, Averlant *et al.* predicted theoretically that one can observe the coexistence of two differently polarized CSs with unequal peak powers and temporal durations [24], and Nielsen *et al.* showed experimentally this kind of coexistence in a monochromatically driven passive Kerr resonator [25]. In this article, we revisit various possible modes of existence of intracavity field dynamics by varying the detuning parameter. In general, there can be two types of polarized solitons, (i) *Group-velocity-locked vector solitons* (GVLVSs) [30–32], where group-velocity mismatch compensates the cross-phase modulation (XPM) effect by mutually shifting their center frequencies in opposite directions and locking the temporal positions irrespective of their polarization states; and (ii) *Polarization-locked vector solitons* (PLVSs) [33,34], where the solitons maintain their polarization state throughout their existence. It is interesting to note that CSs with different polarization properties can be excited in a birefringent fiber-based resonator by only varying the external parameters. One can obtain coexistence of different nonlinear states either by changing the pump power or frequency detuning along one principal axis. Note that such coexistence is a unique feature in a dissipative system, where one of the modes along one principal axis is excited and a significant amount of power is coupled from its orthogonal mode via XPM. In this work, we observe three different types of PLVSs. We carried out a complete analysis of these vector solitons by observing the evolution of their Stokes parameters which inherently signify the amount of flux radiated in different spatial orientations.

*maitrayee@iitkgp.ac.in

†samudra.roy@phy.iitkgp.ac.in

‡skvarshney@ece.iitkgp.ac.in

The complex electric-field distribution in each of these modes has further been calculated with the Jones vector. Stokes and Jones analysis help in deducing several other properties including total polarized flux, degree of linear polarization, and degree of circular polarization in each of these three different cases. The birefringence property of the fiber induces a certain mismatch in the group velocity of the two orthogonally polarized modes. Through rigorous calculations and simulations under various external conditions, it has been observed that soliton propagation in the presence of group-velocity mismatch (GVM) remains inherent to their state of polarization. We believe that our elaborate observations and yet simple conclusions can certainly enrich the understanding of vector CS dynamics.

II. MEAN-FIELD MODEL FOR COUPLED LUGIATO-LEFEVER EQUATION

To study the intracavity field dynamics in a birefringent fiber loop cavity, one can make use of the well-known LLE model. We assume that a single-frequency pump can excite two orthogonal modes which are predominantly coupled via nonlinear XPM. The general form of the coupled LLE in presence of XPM is the following:

$$\tau_R \frac{\partial \psi_{1,2}}{\partial \tau} = \Bigg[-(\alpha + i\nu_{1,2}) + i\gamma L_c(|\psi_{1,2}|^2 + B|\psi_{2,1}|^2) - \beta_{1(\psi_{1,2})} L_c \frac{\partial}{\partial t} - i\frac{\beta_2 L_c}{2}\frac{\partial^2}{\partial t^2}\Bigg]\psi_{1,2} + \sqrt{\theta} P_{1,2}, \tag{1}$$

where $\psi_{1,2}$ are the intracavity fields for two polarization modes. τ is the slow-time which is related to field confinement time in the resonator on a scale of photon lifetime. The term $\beta_{1(\psi_i)}$ is related to group velocity $v_{g(\psi_i)}$ as $\beta_{1(\psi_i)} = v_{g(\psi_i)}^{-1}$. The fast timescale is denoted t, which characterizes the temporal envelope of the pulse in a reference frame moving at the average inverse group velocity $[\bar{\beta}_1 = \frac{1}{2}(\beta_{1(\psi_1)} + \beta_{1(\psi_2)})]$, τ_R is the round trip time within the cavity. The slow-timescale and fast-timescale are interconnected through $E(\tau = m\tau_R, t) = E^{(m)}(0, t)$, where m is the index number of the round trips. We consider that both the modes suffer equal loss α. The group-velocity dispersion (GVD) coefficient $\beta_2 < 0$ and nonlinear coefficient γ of the fiber are assumed to be the same [35] for two orthogonal polarization modes as the cavity is pumped with a single frequency. These two orthogonal modes are coupled with nonlinear XPM. The XPM coupling factor is $B = \frac{2}{3}$ for linearly birefringent fibers. Due to the modal birefringence, two orthogonal components experience different group velocities, i.e., $\beta_{1(\psi_1)} \neq \beta_{1(\psi_2)}$ in general. In this case, frequency detuning $(\nu_{1,2})$ between the driving field $P_{1,2}$ and the nearest cavity resonance are different, i.e., $\nu_1 \neq \nu_2$, $P_{1,2}$ are the driving field amplitudes given by $P_1 = P\cos(\phi)$ and $P_2 = P\sin(\phi)$, where ϕ is the linear polarization direction of the input beam with respect to slow-axis orientation of the birefringent fiber. θ denotes the power transmission coefficient from coupler to the resonator, and the length of the resonator is L_c. We introduce the rescaling factors $\tau \to \alpha\tau/\tau_R, t \to t(2\alpha/|\beta_2|L_c)^{1/2}$, $\psi_{1,2} \to \psi_{1,2}(\gamma L_c/\alpha)^{1/2}$, $P_{1,2} \to P_{1,2}(\gamma L_c\theta/\alpha^3)^{1/2}$, $\sigma_{1,2} = \nu_{1,2}/\alpha$, represents the normalized detuning frequencies and $\delta = (\beta_{1(\psi_1)} - \beta_{1(\psi_2)})\sqrt{\frac{L_c}{2\alpha|\beta_2|}}$ denotes the GVM between two orthogonal polarization modes. Using these rescaling factors in Eq. (1), we obtain following form of normalized coupled LLE:

$$\frac{\partial \psi_1}{\partial \tau} = \Bigg[-(1 + i\sigma_1) + i\left(|\psi_1|^2 + \frac{2}{3}|\psi_2|^2\right) + \delta\frac{\partial}{\partial t} + i\frac{\partial^2}{\partial t^2}\Bigg]\psi_1 + P\cos(\phi), \tag{2}$$

$$\frac{\partial \psi_2}{\partial \tau} = \Bigg[-(1 + i\sigma_2) + i\left(|\psi_2|^2 + \frac{2}{3}|\psi_1|^2\right) - \delta\frac{\partial}{\partial t} + i\frac{\partial^2}{\partial t^2}\Bigg]\psi_2 + P\sin(\phi). \tag{3}$$

The coupled LLE mentioned in Eq. (1) neglects the effect of higher-order dispersion, linear mode coupling, and the coherent four-wave mixing (FWM) term [24].

III. STEADY AND HOMOGENEOUS SOLUTION OF COUPLED LUGIATO-LEFEVER MODEL

The homogeneous steady-state (HSS) conditions of Eqs. (2) and (3) satisfying $\frac{\partial \psi_{1,2}}{\partial \tau} = \frac{\partial^n \psi_{1,2}}{\partial t^n} = 0$ lead to nine different solutions for an individual set of external parameters $(\sigma_{1,2}, P_{1,2})$. The coupled HSS equations take the following form [11,36]:

$$X^3 + X^2\left(\frac{4}{3}Y - 2\sigma_1\right) + X\left(1 + \sigma_1^2 + \frac{4}{9}Y^2 - \frac{4}{3}\sigma_1 Y\right) = G_1, \tag{4}$$

$$Y^3 + Y^2\left(\frac{4}{3}X - 2\sigma_2\right) + Y\left(1 + \sigma_2^2 + \frac{4}{9}X^2 - \frac{4}{3}\sigma_2 X\right) = G_2, \tag{5}$$

where $X = |\psi_1|^2$, $Y = |\psi_2|^2$, $G_1 = |P|^2\cos^2(\phi)$, $G_2 = |P|^2\sin^2(\phi)$. Although analytical solutions are not possible for these coupled LLEs, one can certainly estimate HSS features from Fig. 1 showing total HSS intracavity field as a function of external parameters like detuning and pump power. In Fig. 1(a), we plot total HSS solution $(|\psi|^2 = |\psi_1|^2 + |\psi_2|^2)$ as a function of σ_1 keeping equal pump power $(\phi = \pi/4)$ to each orthogonal mode. We observe that the cavity resonance is tilted and also split in presence of a detuning mismatch $\Delta\sigma = \sigma_2 - \sigma_1$ between two orthogonal modes. One can interpret that different nonlinear states can simultaneously coexist from the overlap of two resonances corresponding to two peaks. We have marked three different detuning values on this HSS resonance curve for which we observe the three different coexisting nonlinear states shown in Figs. 1(c)–1(e). In Fig. 1(b) we plot the total HSS field as a function of external pump power P while individual detuning is fixed. The two negative slopes are unconditionally unstable (marked with filled circles) and the three positive slopes are stable against homogeneous perturbations. The position and width of these two bistable (A-B, C-D) regions can be well manipulated with external detunings [24]. In a passive resonator, the growing modulation instability (MI) pattern eventually stabilizes due to dissipation, which ultimately forms a stationary periodic pattern [18]. In Fig. 1(c) for

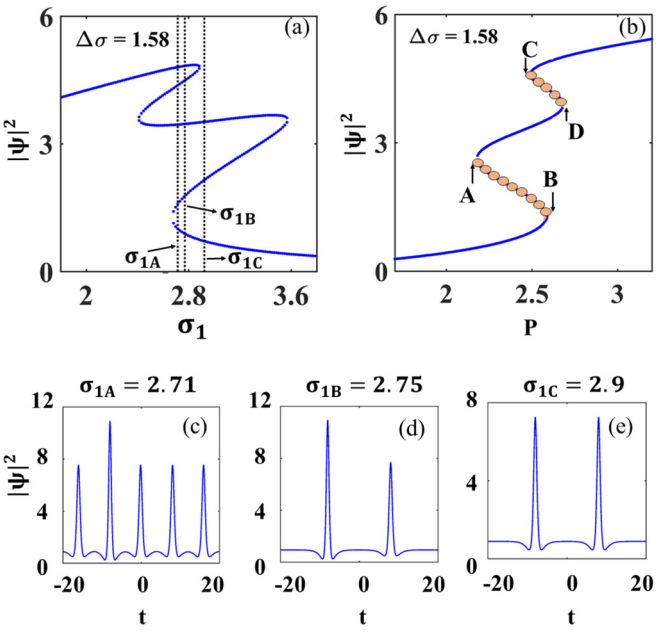

FIG. 1. (a) Total intracavity field (HSS solution; $|\psi|^2 = |\psi_1|^2 + |\psi_2|^2$) as a function of detuning (σ_1, σ_2), where $\Delta\sigma = \sigma_2 - \sigma_1$ with equal pump power ($P_1 = P_2 = 2.54$) in both orthogonal modes. (b) HSS solution as a function of pump power P with the same detuning mismatch $\Delta\sigma$. Solid lines showing the stable solutions, negative slopes (filled circles) represent unstable branches. (c)–(e) Stationary field profile obtained from coupled LLE at selected detunings [shown with dotted lines in panel (a)] depicting coexistence of different nonlinear states. (c) MI and CS coexistence, $\sigma_{1A} = 2.71$. (d) Coexistence of two nonidentical CSs, $\sigma_{1B} = 2.75$. (e) Coexistence of two identical CSs, $\sigma_{1C} = 2.9$.

$\sigma_{1A} = 2.71$, we observe the coexistence of a stable MI pattern and a CS which was recently observed experimentally [25]. In Fig. 1(d) for $\sigma_{1B} = 2.75$, we observe two nonidentical CSs (peak power and polarization properties) and in Fig. 1(e) for $\sigma_{1C} = 2.9$, we observe the coexistence of two identical CSs in two orthogonal modes.

IV. ANALYSIS OF THE POLARIZATION PROPERTIES OF CAVITY SOLITONS

In this section, we analyze the dynamics of the coexisting CSs in the fiber-based cavity and their intrinsic polarization properties. Due to the birefringence of the fiber, two orthogonal modes with two different resonance frequencies can be simultaneously excited with a single linearly polarized light. The amplitudes of the driving field in individual modes can be controlled externally by the projection angle ϕ with respect to the slow-axis orientation. Note that the frequency detuning for two modes are in general unequal ($\sigma_1 \neq \sigma_2$). In a very recent experimental work [25], control over detuning parameters ($\Delta\sigma$) with the help of a polarization controller (PC) in a cavity has been achieved. In the present work, we consider the polarization properties of CSs with equal driving power ($\phi = \pi/4$) and small detuning mismatch ($\Delta\sigma \approx 1$). With the choice of external parameters, we observe PLVSs. Numerical results reveal that CS dynamics in the presence of GVM can be well predicted from their inherent polarization state.

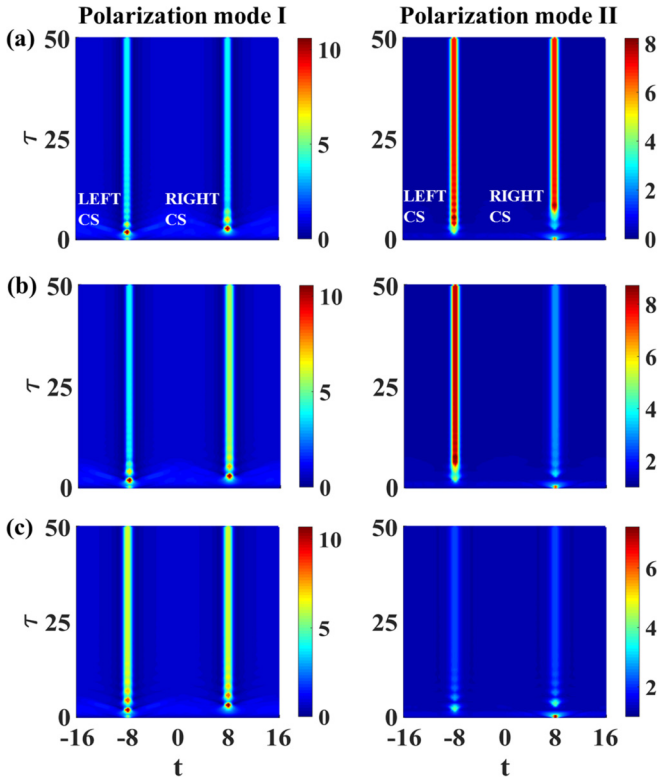

FIG. 2. Coexistence of CSs in both orthogonal polarization modes with variations in detuning mismatch ($\Delta\sigma = \sigma_2 - \sigma_1$) between two modes: $\sigma_1 = 2.75$, (a) $\sigma_2 = 4.2$, identical CSs; (b) $\sigma_2 = 4.32$, nonidentical CSs; (c) $\sigma_2 = 4.5$, identical CSs. Identical coexisting CSs in panels (a) and (c) differ by their polarization states.

A. Case I: Zero group-velocity mismatch ($\delta = 0$)

In this subsection, we investigate the polarization dynamics of two coexisting CSs considering zero GVM ($\delta = 0$) between two orthogonal modes. We numerically solve the set of coupled differential equations (2) and (3). Different polarization states are obtained by varying the cavity detuning σ_2 along one orthogonal mode while keeping the other detuning σ_1 fixed. We choose the initial field in the form of a sech pulse resting over a cw background, as mentioned below:

$$\psi_{10} = \psi_{1_{\rm hom}} + \sqrt{2\sigma_1}\,\mathrm{sech}(\sqrt{(1+B)2\sigma_1}(t+t_0)), \quad (6)$$

$$\psi_{20} = \psi_{2_{\rm hom}} + \sqrt{2\sigma_2}\,\mathrm{sech}(\sqrt{(1+B)2\sigma_2}(t-t_0)), \quad (7)$$

where $\psi_{1_{\rm hom}} = P\cos(\phi)/\sigma_1^2$, $\psi_{2_{\rm hom}} = P\sin(\phi)/\sigma_2^2$, $B = \frac{2}{3}$, and t_0 denotes initial delay. At first, we excite only one mode along each orthogonal axis and the nonlinear interaction leads to a steady state in the resonator where we observe a coexistence of both modes along individual orthogonal axes. Due to XPM, each CS sheds some of its energy into its orthogonal counterpart such that either two identical (equal amplitude and width) CSs or nonidentical (both different amplitude and width) CSs coexist along each orthogonal axis. In Fig. 2, we demonstrate the evolution of two coexisting CS states by changing the detuning σ_2 along one of the orthogonal axes. For polarization mode I (II) we launch ψ_{10} and ψ_{20} along two polarization axes and capture the evolution of $|\psi_{10}|^2$ ($|\psi_{20}|^2$) over slow time τ. We notice, at initial stage, that the energy

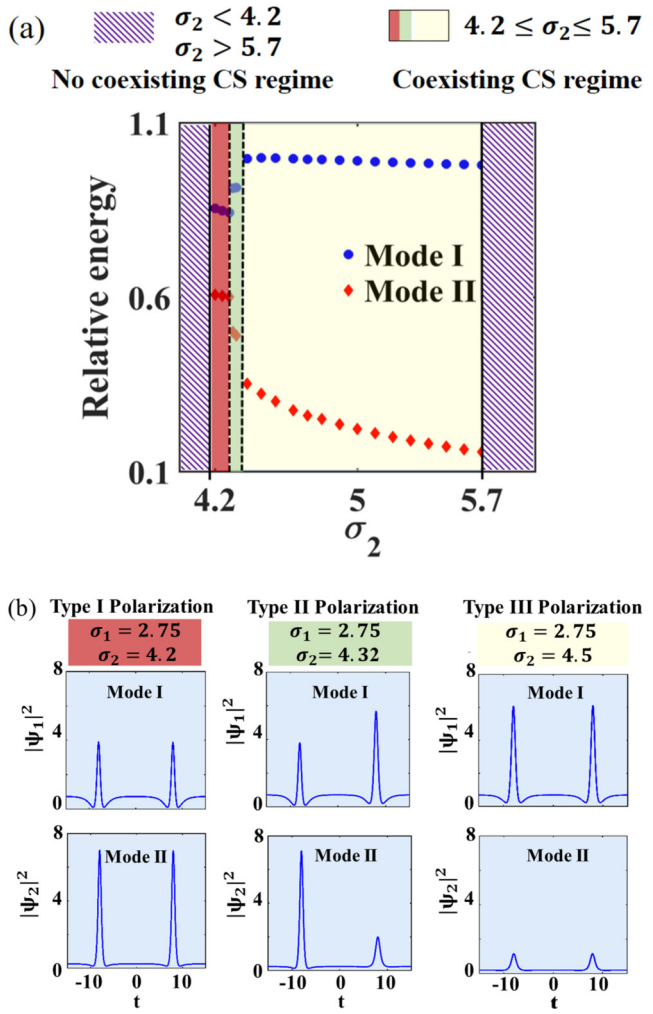

FIG. 3. (a) Relative energy ($E_{1,2}/E_{\max}$) of two orthogonal polarization modes [filled circles (mode I) and filled squares (mode II)] as a function of detuning frequency σ_2. Patterned regions ($\sigma_2 < 4.2$ and $\sigma_2 > 5.7$) do not contain coexisting CSs. Three types of polarization states have been marked in the region $4.2 \leqslant \sigma_2 \leqslant 5.7$ (shaded region) corresponding to three distinct energy levels. (b) Power distribution in the form of coexisting CSs with cw background in individual orthogonal modes. CSs are either identical (amplitude, polarization state) (type I and type III) or nonidentical (type II).

is periodically transferred from one mode to other and finally stabilizes. We identify three distinct coexisting CSs based on their polarization states. As illustrated in Fig. 2, a pair of identical [see Figs. 2(a) and 2(c)] or nonidentical CSs [see Fig. 2(b)] are emerged depending on the value of detuning mismatch $\Delta\sigma = \sigma_2 - \sigma_1$ along each orthogonal mode. In Fig. 3(a), we evaluate the energy ($E_{1,2} = \int |\psi_{1,2}|^2 dt$) associated with two orthogonal modes as a function of detuning parameter σ_2. Filled circles and filled squares indicate the relative energy levels of mode I and mode II, respectively. Using the E-σ_2 diagram we can map the polarization states (type I, type II, and type III) of the individual CS pairs. The three distinct relative energy levels ($E_{1,2} \rightarrow E_{1,2}/E_{\max}$) in each orthogonal mode indicate a change of polarization state. An iterative simulation for $\sigma_1 = 2.75$ reveals that the coexisting CS can emerge in the range $4.2 < \sigma_2 < 5.7$. No CS pairs are observed in the patterned regions corresponding to either $\sigma_2 < 4.2$ or $\sigma_2 > 5.7$, which marks the lower and upper boundary limits to observe coexisting CSs. In Fig. 3(b), we illustrate the existence of CS pairs having different polarization states. Identical soliton pairs emerge in the first (type I) and third (type III) window where the power distribution is equal. A distinct nonidentical CS pair evolves in the second window (type II) with unequal power distribution. To characterize and analyze the polarization states of the intracavity field, we exploit three well-known properties: (i) Stokes parameters, (ii) Jones vectors, and (iii) polarization ellipse, associated with each case. Stokes parameters are a convenient way of expressing the polarization state of any unpolarized, partially polarized, or fully polarized beams. The Stokes parameters contain four real quantities which can be calculated numerically by solving a coupled LLE. The four real quantities are defined as $S_0 = |\psi_1|^2 + |\psi_2|^2$, $S_1 = |\psi_1|^2 - |\psi_2|^2$, $S_2 = \psi_1^*\psi_2 + \psi_1\psi_2^*$, and $S_3 = i(\psi_1^*\psi_2 - \psi_1\psi_2^*)$. Physically, these parameters signify the amount of flux radiated in space along different orientations. One can write this in the following form [37]:

$$S = \begin{pmatrix} S_0 \\ S_1 \\ S_2 \\ S_3 \end{pmatrix} = \begin{pmatrix} P_H + P_V \\ P_H - P_V \\ P_{\pi/4} - P_{3\pi/4} \\ P_R - P_L \end{pmatrix}, \tag{8}$$

where S_0 signifies the total irradiance of the light beam, S_1 corresponds to the difference between horizontal- and vertical-polarized flux components, and S_2 denotes flux components along the $\pi/4$ and $3\pi/4$ orientations. Therefore, a positive S_2 signifies an excess of net flux along the $\pi/4$ direction and is negative if $P_{3\pi/4} > P_{\pi/4}$. Similarly S_3 measures the difference between right (P_R) and left (P_L) circularly polarized flux components. In Fig. 4, we plot the S parameters for three different cases of coexisting CSs by solving Eqs. (2) and (3) numerically for three different sets of detuning parameters (σ_1, σ_2), with the help of the split-step Fourier method. From Figs. 4(a) and 4(c), we observe two CSs along two orthogonal principal axes correspond to similar S parameters. For type I, both the CSs are dominated by the linear flux component with vertical polarization ($S_1 < 0$) and $\pi/4$ polarization ($S_2 > 0$), whereas in type III both CSs are dominated by linear flux component with horizontal polarization ($S_1 > 0$) and $3\pi/4$ polarizations ($S_2 < 0$), whereas both above-mentioned types of CSs have similar circular polarization (left circular $S_3 < 0$). For the case of nonidentical CSs (type II), the S parameters are nonidentical, either in magnitude (S_0 and S_3) or both in magnitude as well as polarization orientations (S_1 and S_2). Exploiting the S-parameter analysis, we calculate several other properties related with the output polarization state of the light beam. When a linearly polarized light is launched, the output electric field associated with the individual CS is also fully polarized. One can be assured by calculating the degree of polarization (DoP), which characterizes the randomness of a polarization state [37]:

$$DoP(S) = \frac{\sqrt{S_1^2 + S_2^2 + S_3^2}}{S_0}, \quad 0 \leqslant DoP \leqslant 1. \tag{9}$$

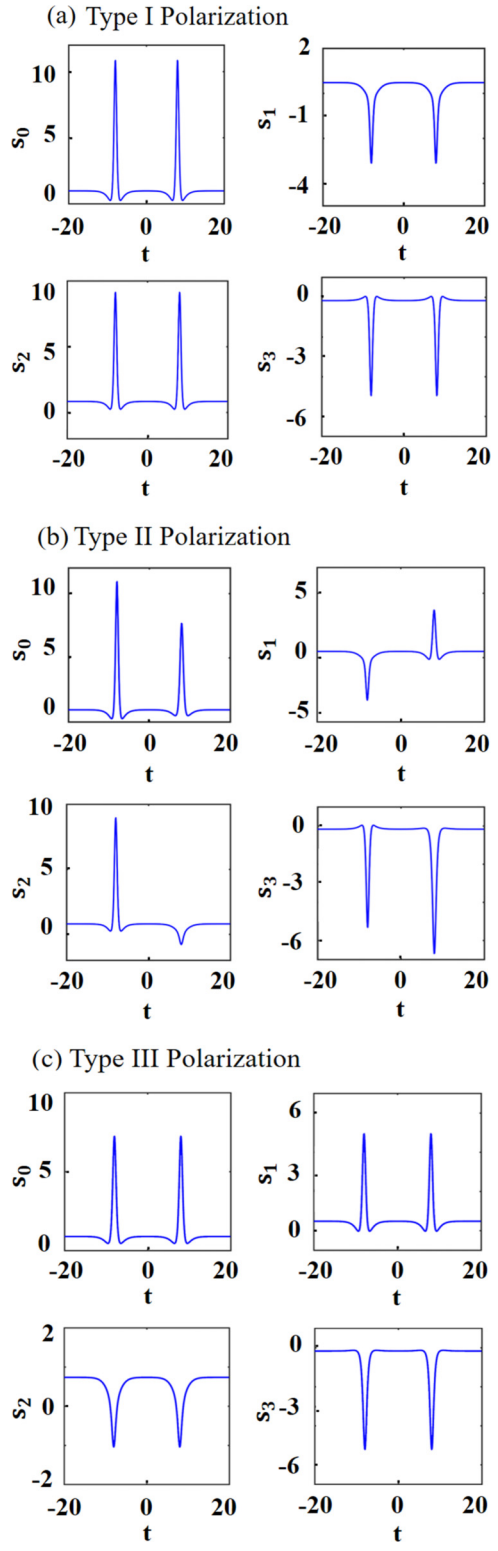

FIG. 4. Stokes parameters for three different polarized states with $\sigma_1 = 2.75$. (a) $\sigma_2 = 4.2$, (b) $\sigma_2 = 4.32$, and (c) $\sigma_2 = 4.5$, numerically obtained by solving Eqs. (2) and (3). S_0 represents total flux whereas S_1 and S_2 dictate flux from linearly polarized components, and S_3 denotes the circularly polarized flux component.

In each case, we numerically calculate the *DoP* and observe its value as one, which confirms that the output light is fully polarized. With the help of these S parameters, one can also identify several other characteristics such as the total flux associated with individual CSs in each of these three cases. Total polarized flux is defined by $(S_1^2 + S_2^2 + S_3^2)^{1/2}$. The degree of linear polarization (DoLP) $(S_1^2 + S_2^2)^{1/2}/S_0$ signifies the amount of polarization confined in a plane. We calculate the DoLP in every case and find that it is neither zero (fully circularly polarized) nor one (fully linearly polarized), which means that both CSs are elliptically polarized. Furthermore, we calculate the degree of circular polarization (DoCP) by using $\frac{S_3}{S_0}$, which characterizes the amount of flux polarized in circular (left or right) orientation. The ellipticity ϵ of the polarization ellipse,

$$\frac{|S_3|}{\sqrt{S_1^2 + S_2^2 + S_3^2} + \sqrt{S_1^2 + S_2^2}} = \frac{b}{a},$$

is a measure of the ratio of the minor axis to the major axis. Numerical values for all three cases are listed in Table I. While the S parameters provide detailed information about the polarization state of the output field, they do not provide phase information about the complex electric field associated with the CS. To extract the phase information, we rely on a Jones vector analysis. The Jones vector comprises two complex electric-field vectors and also indicates the polarization state of the field. Because we deal with two orthogonal modes of the system, the Jones vectors can be written as

$$J(\psi_1) = \begin{pmatrix} A_{1,x}e^{-i\chi_{1,x}} \\ A_{1,y}e^{-i\chi_{1,y}} \end{pmatrix}, \quad J(\psi_2) = \begin{pmatrix} A_{2,x}e^{-i\chi_{2,x}} \\ A_{2,y}e^{-i\chi_{2,y}} \end{pmatrix}, \tag{10}$$

where $\psi_1 = A_{1,j}e^{-i\chi_{1,j}}$ and $\psi_2 = A_{2,j}e^{-i\chi_{2,j}}$, $j = x, y$. Each Jones vector has four degrees of freedom, two indicating their amplitudes (A_x, A_y) and two corresponding to their phase (χ_x, χ_y). One can therefore easily create the polarization ellipse. For an elliptically polarized state, the ellipse is traced by the tip of the electric-field vector as a function of time. The Stokes parameter and Jones vector are related to the polarization dynamics of the output field, so they can be interlinked as

$$S = \frac{\epsilon_0 c}{2}\begin{pmatrix} A_x^2 + A_y^2 \\ A_x^2 - A_y^2 \\ 2A_xA_y\cos(\chi_x - \chi_y) \\ 2A_xA_y\sin(\chi_x - \chi_y) \end{pmatrix} = \begin{pmatrix} S_0 \\ S_1 \\ S_2 \\ S_3 \end{pmatrix}.$$

We follow the sign convention of Ref. [37] which considers right-circular polarization as positive for Stokes parameters and left-circular polarization as positive for the Jones vector. The factor $\frac{\epsilon_0 c}{2}$ is introduced just to balance the units and further considered as one, because it only acts as a scaling factor for the numerical values. From the above matrix we find

$$A_x = \sqrt{\frac{S_0 + S_1}{2}}, \quad A_y = \sqrt{\frac{S_0 - S_1}{2}}, \tag{11}$$

$$\chi_x - \chi_y = \tan^{-1}\frac{S_3}{S_2}. \tag{12}$$

Exploiting the above information one can draw the polarization ellipse, which must be confined in a box with area $[2A_x \times 2A_y]$. Using Eqs. (11) and (12), we find the Jones

TABLE I. Polarization properties of generated CSs for three different sets of detuning parameters.

Measured quantities	Type I $\sigma_1 = 2.75, \sigma_2 = 4.2$	Type II $\sigma_1 = 2.75, \sigma_2 = 4.32$		Type III $\sigma_1 = 2.75, \sigma_2 = 4.5$
	Identical CS	Left CS	Right CS	Identical CS
S parameters	$S_0 = 10.83, S_1 = -3.09$ $S_2 = 9.09, S_3 = -4.99$	$S_0 = 10.92\ S_1 = -3.31$ $S_2 = 8.92, S_3 = -5.36$	$S_0 = 7.63, S_1 = 3.73$ $S_2 = -0.81, S_3 = -6.61$	$S_0 = 7.23, S_1 = 4.94$ $S_2 = -1.04, S_3 = -5.18$
Polarized flux	10.83	10.92	7.63	7.23
Degree of linear polarization (DoLP)	0.89	0.87	0.50	0.69
Degree of circular polarization (DoCP)	−0.46	−0.49	−0.87	−0.72
Ellipticity	0.24	0.26	0.58	0.42

vectors in terms of S parameters as follows:

$$J(\psi_{1,2}) = \begin{pmatrix} \sqrt{\frac{S_0+S_1}{2}} \\ \sqrt{\frac{S_0-S_1}{2}} e^{i\tan^{-1}\left(\frac{S_3}{S_2}\right)} \end{pmatrix}. \tag{13}$$

From Table II, one can obtain required information of polarization ellipse for three different cases and also the corresponding flux distribution in different spatial orientations. In Fig. 5 we illustrate the graphical representation of the polarization states for three different types of coexisting CSs. We observe that all ellipses are left-circularly polarized, as indicated by the arrowhead, which is also obvious from the fourth column in each case that shows that the diameter of the left-circular flux is larger than that of the right-circular flux ($P_L > P_R$). The part of the total linear polarization components are indicated by $P_{H,V}$ and $P_{\pi/4,3\pi/4}$ components. The length of the vectors in each case signifies the strength of the flux component along that direction. In Fig. 5(a) (type-I), both CSs are dominated by vertical ($P_V > P_H$) and along 45° polarized ($P_{\pi/4} > P_{3\pi/4}$) flux components, Figs. 5(b) and 5(c) represent type-II polarization where two nonidentical CSs coexist; the left CS is vertically ($P_V > P_H$) and along 45° polarized ($P_{\pi/4} > P_{3\pi/4}$) [Fig. 5(b)], whereas the right CS is horizontally ($P_V < P_H$) and along 135° polarized ($P_{\pi/4} < P_{3\pi/4}$) [Fig. 5(c)]. In Fig. 5(d) we observe identical CSs (type-III), both dominated by horizontal ($P_V < P_H$) and along 135° polarized ($P_{\pi/4} < P_{3\pi/4}$) flux components. From the basis vectors of Stokes parameters or Jones vectors, one can obtain the magnitude of these flux components, shown in Appendix.

B. Case II: Finite group-velocity mismatch ($\delta \neq 0$)

A fiber with constant modal birefringence ($B_m = |n_1 - n_2|$) has two principal axes along which it can maintain the linear-polarized state of input cw light. We assume $n_1 > n_2$, where n_1 and n_2 are the mode indexes along the slow and fast axes, respectively. Depending on the beat length ($L_B = \frac{\lambda}{B_m}$), which is typically ≈1 cm for high-birefringent fiber and ≈1 m [16] for low-birefringent fiber, one may need to consider the effect of GVM while considering CS propagation in birefringent fiber. For $\delta \neq 0$ in the coupled equations (2) and (3), we consider the effect of GVM on CS dynamics along the slow and fast axes. In Fig. 6 we plot the dynamics of type-I and type-III coexisting CSs. We observe an identical monotonic temporal drift of two CSs which is influenced by the GVM term. One can correlate their direction of propagation with their inherent linear polarization state. For Fig. 6(a), both CSs are dominated by a 45° linear polarized component ($P_{\pi/4} > P_{3\pi/4}$), whereas for the case in Fig. 6(b) both CSs are dominated by a 135° linear polarized component ($P_{\pi/4} < P_{3\pi/4}$). The numerical simulation reveals that, in presence of GVM ($\delta \neq 0$), both CSs either slow down [when the CSs are 45° linearly polarized, Fig. 6(a)] or speed up (when the CSs are 135° linearly polarized, Fig. 6(b)], depending on their inherent linearly polarized state. In Figs. 6(c) and 6(d) we show the velocity of a CS (v_{cs}) as a function of the GVM parameter ranging from a low-birefringence value ($\delta = 0.01$) to a high-birefringence value ($\delta = 0.3$) [35,38,39]. For type-I polarization in Fig. 6(c), the velocity increases monotonically as the GVM increases, whereas the opposite pattern is observed in the case of type-III polarization in Fig. 6(d) where velocity decreases monotonically as we increase the GVM. Next, we investigate the dynamics of two nonidentical CSs which have type-II polarization. In Fig. 7, we show the case ($\sigma_1 = 2.75$, $\sigma_2 = 4.32$) where two coexisting nonidentical CSs evolve over several round-trips. We vary the GVM parameter from a very low value ($\delta = 0.01$) to a higher value ($\delta = 0.2$) and observe different evolution dynamics. To capture the role of polarization state on the temporal dynamics of the soliton pair,

TABLE II. Parameters for polarization ellipse and the corresponding decomposed spatial polarized flux distribution.

Type I $\sigma_1 = 2.75, \sigma_2 = 4.2$	Type II $\sigma_1 = 2.75, \sigma_2 = 4.32$		Type III $\sigma_1 = 2.75, \sigma_2 = 4.5$
Identical CS	Left CS	Right CS	Identical CS
$J(\psi_{1,2} = \begin{pmatrix} 1.97 \\ 2.64e^{-0.5i} \end{pmatrix}$	$J(\psi_1) = \begin{pmatrix} 1.95 \\ 2.67e^{-0.54i} \end{pmatrix}$	$J(\psi_2) = \begin{pmatrix} 2.38 \\ 1.39e^{1.45i} \end{pmatrix}$	$J(\psi_{1,2}) = \begin{pmatrix} 2.47 \\ 1.07e^{1.37i} \end{pmatrix}$
$P_H = 3.87, P_V = 6.96$	$P_H = 3.81, P_V = 7.11$	$P_H = 5.68, P_V = 1.95$	$P_H = 6.08, P_V = 1.15$
$P_{\pi/4} = 9.96, P_{3\pi/4} = 0.87$	$P_{\pi/4} = 9.92, P_{3\pi/4} = 0.99$	$P_{\pi/4} = 3.41, P_{3\pi/4} = 4.22$	$P_{\pi/4} = 3.09, P_{3\pi/4} = 4.14$
$P_L = 7.91, P_R = 2.92$	$P_L = 8.14, P_R = 2.78$	$P_L = 7.12, P_R = 0.51$	$P_L = 6.20, P_R = 1.03$

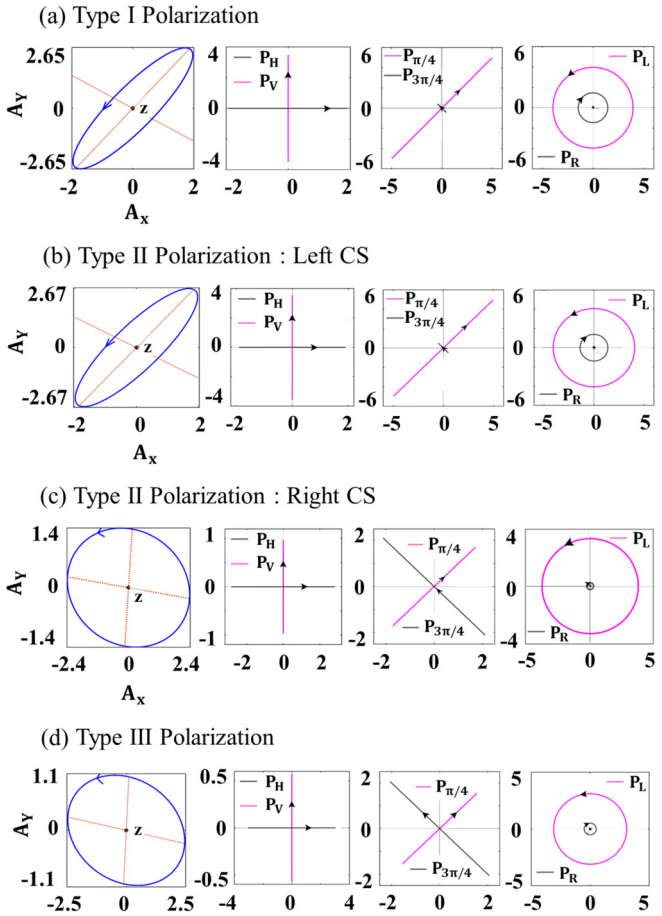

FIG. 5. Analysis of polarization states for three types of coexisting CSs with $\sigma_1 = 2.75$; (row-wise) polarization ellipse, flux components in horizontal-vertical orientation, $\pi/4$-$3\pi/4$ orientation, left-right circular orientation. (a) ($\sigma_2 = 4.2$) Type-I identical CS state. (b), (c) Type-II nonidentical CS state ($\sigma_2 = 4.32$): (b) left CS (c) right CS. (d) Type-III identical CS state ($\sigma_2 = 4.5$).

we numerically calculate the S parameters at two different propagation stages. Our simulation reveals that the GVM does not affect the helicity or state of circular polarization because S_3 is always negative (left-circularly polarized) in all three cases. In Fig. 7(a) we demonstrate that two coexisting CSs evolve at different velocities. In the presence of small GVM ($\delta = 0.01$), the fast-axis CS (left CS) and the slow-axis CS (right CS) either slow down or accelerate, respectively. We find that the fast-axis CS is dominated by $\pi/4$ polarization (as $S_2 > 0$) whereas the slow-axis CS is dominated by $3\pi/4$ polarization (as $S_2 < 0$). After a long evolution, the relative velocity of the two coexisting CSs becomes fixed around $\tau \approx 1400$ but maintains its initial polarization state. In Fig. 7(b), we show the CSs dynamics for medium birefringence ($\delta = 0.1$). We simulate the dynamics of CS pairs for a range of GVM values $0.02 < \delta < 0.13$. It is observed that two orthogonally polarized CSs evolve with different velocities and experience a sharp change in their velocities around $\tau \approx 160$ for the given set of external parameters. For $\tau > 160$, two CSs propagate with identical velocity by forming a merged state. It is observed that the dominated linear polarized flux component $P_{3\pi/4}$ translates into $P_{\pi/4}$ for the slow-axis CS, and

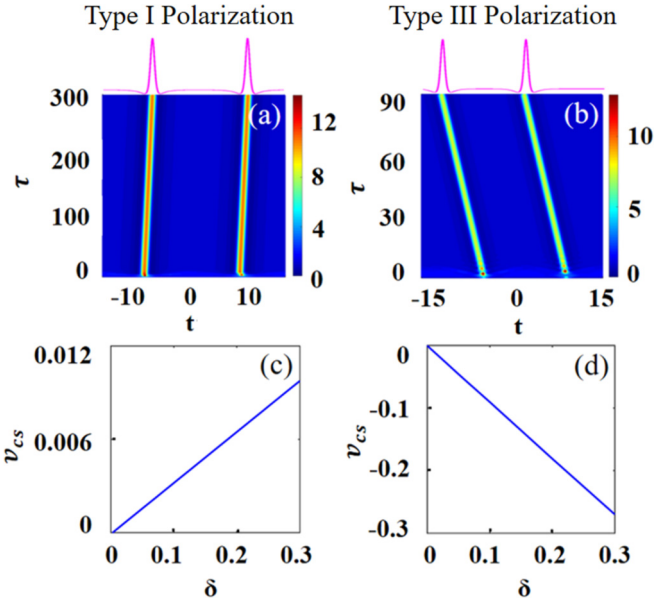

FIG. 6. (a), (b) Mesh plot of total power $|\psi|^2$ in presence of group-velocity mismatch (GVM = 0.1) for coexisting identical CSs. (a) Type-I polarization: $\sigma_1 = 2.75$, $\sigma_2 = 4.2$, corresponding to $S_2 > 0$. (b) Type-III polarization: $\sigma_1 = 2.75$, $\sigma_2 = 4.5$, corresponding to $S_2 < 0$. Velocity profile of CS as a function of GVM for (c) Type-I polarization and (d) Type-III polarization.

also the amount of circular flux component varies within two orthogonal modes (along the fast and slow axes) in a merged state beyond $\tau \approx 160$. In Fig. 7(c), we further increase the value of GVM ($\delta = 0.2$), which signifies a high-birefringence value. We notice that two nonidentical CS eventually form a stable identical soliton pair. We also notice that the initial linear polarization state of the slow CS flips after a certain round trip evolution around $\tau \approx 50$. Not only does the orientation of the linear polarized flux components flip, but it also becomes identical with the fast CS. Upon further increasing the value of δ for this nonidentical coexisting CSs state, we observe a similar scenario as mentioned in Fig. 7(c), only the flipping occurs at a smaller τ value. From this detailed analysis, we conclude that, in a weakly birefringent fiber, one can observe the coexistence of identical and nonidentical polarized CS states by properly selecting the external parameters. The dynamics of the CS pair can be well interpreted by analyzing their inherent polarization state. We also point out that it is very unlikely to observe the coexistence of nonidentical CSs in a resonator made from a high-birefringent fiber when both orthogonal modes of the fiber are equally pumped.

V. CONCLUSION

We have studied theoretically the polarization dynamics of vector CSs in a birefringent fiber resonator. With the help of coupled LLEs, we observe the coexistence of identical and nonidentical CSs in both orthogonal modes which are coupled via nonlinear XPM. Different detuning mismatch between the resonator eigenmode and the external pump mode can lead to the generation of CSs with different polarization properties. With the help of Stokes parameters and the Jones vector, we

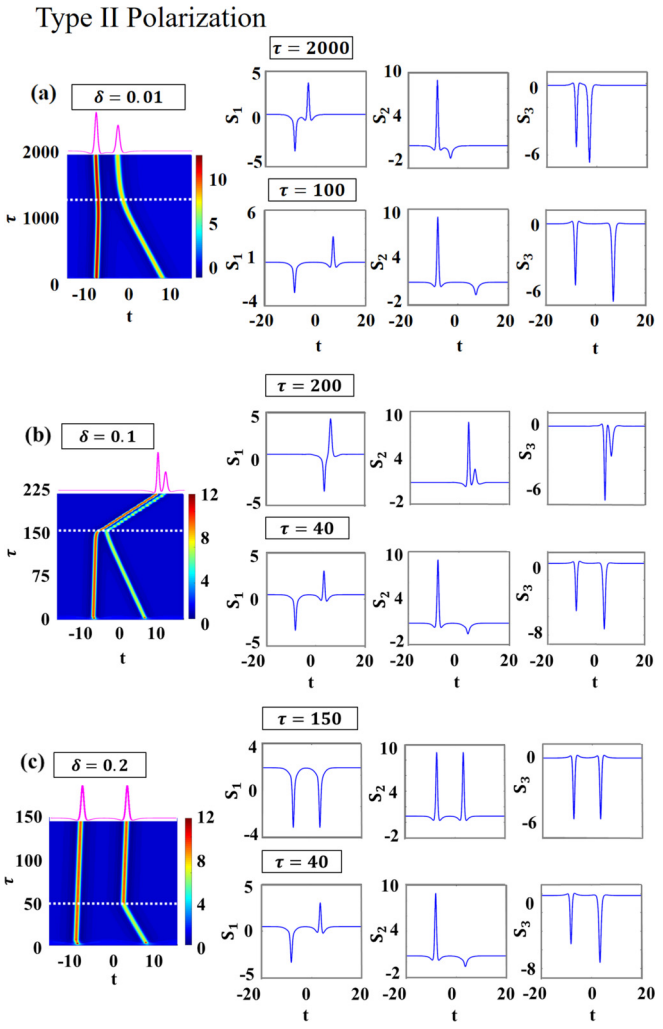

FIG. 7. Total power ($|\psi|^2$) in the presence of GVM for coexisting nonidentical CSs with $\sigma_1 = 2.75$, $\sigma_2 = 4.32$ along with the evolution of the S parameters (S_1, S_2, S_3). (a) GVM = 0.01, both CSs maintain their state of polarization. (b) GVM = 0.1, around $\tau \approx 160$ the slow-axis CS (right one) changes its polarization state (S_2 flips sign) but both remain nonidentical. (c) GVM = 0.2, around $\tau \approx 50$ the polarization state of the slow-axis CS (right one) changes and the two CSs become identical.

analyze in detail the polarization states of generated CSs. Furthermore, we incorporate the effects of group-velocity mismatch (GVM) between the fast- and the slow-moving component in each of these coexisting identical and nonidentical CSs. In spite of GVM between the two CSs, identical CSs behave in the same fashion. They either slow down or accelerate depending on their linear polarization state. For nonidentical CSs, the slow-axis CS changes its linear polarization state for a higher GVM value after a certain time of confinement in such a way that both CSs become identical in the steady state. Thus, it is unfavorable to observe nonidentical coexisting CSs in the case of a high-birefringent fiber resonator while two orthogonal modes are equally pumped. We believe that these findings will certainly enrich the fundamental understanding of the polarization properties of dissipative solitons based on passive resonators.

TABLE III. Basis of Stokes parameters and Jones vector.

Polarization types	Symbol	Stokes parameters	Jones vector
Horizontal linear	H	(1,1,0,0)	(1,0)
Vertical linear	V	(1, −1, 0, 0)	(0,1)
45° linear	$\pi/4$	(1,0,1,0)	$(1, 1)/\sqrt{2}$
135° linear	$3\pi/4$	(1, 0, −1, 0)	$(1, -1)/\sqrt{2}$
Right circular	R	(1,0,0,1)	$(1, -i)/\sqrt{2}$
Left circular	L	(1, 0, 0, −1)	$(1, i)/\sqrt{2}$

ACKNOWLEDGMENTS

The author M.S. would like to thank the Ministry of Human Resource Development, Government of India and IIT Kharagpur for financial support to carry out her research work. The author S.K.V. acknowledges the support received from project vide sanction no. DST/NM/NNETRA/2018(6)-IITKGP.

APPENDIX: CALCULATIONS OF THE POLARIZATION FLUX MEASUREMENT

The Stokes parameters and Jones vector are two parallel approaches to measure the polarization properties of a light beam. To obtain the six fundamental polarization flux components (P_H, P_V, $P_{\pi/4}$, $P_{3\pi/4}$, P_R, P_L), we need to use the basis of each representation, as shown in Table III. With the help of these basis vectors and using the form of A_x, A_y and $\chi_x - \chi_y$ obtained in Eqs. (11) and (12), one can readily derive the flux in different orientations as follows:

$$P_H = \frac{S_0 + S_1}{2} = \frac{\epsilon_0 c}{2} A_x^2, \tag{A1}$$

$$P_V = \frac{S_0 - S_1}{2} = \frac{\epsilon_0 c}{2} A_y^2, \tag{A2}$$

$$P_{\pi/4} = \frac{S_0 + S_2}{2} = \frac{\epsilon_0 c}{2}\left(\frac{A_x^2 + A_y^2}{2} + A_x A_y \cos\chi\right), \tag{A3}$$

$$P_{3\pi/4} = \frac{S_0 - S_2}{2} = \frac{\epsilon_0 c}{2}\left(\frac{A_x^2 + A_y^2}{2} - A_x A_y \cos\chi\right), \tag{A4}$$

$$P_R = \frac{S_0 + S_3}{2} = \frac{\epsilon_0 c}{2}\left(\frac{A_x^2 + A_y^2}{2} + A_x A_y \sin\chi\right), \tag{A5}$$

$$P_L = \frac{S_0 - S_3}{2} = \frac{\epsilon_0 c}{2}\left(\frac{A_x^2 + A_y^2}{2} - A_x A_y \sin\chi\right), \tag{A6}$$

where $\chi = \chi_x - \chi_y$. During the calculation of the flux components, we have taken the scaling factor $\frac{\epsilon_0 c}{2}$ to be unity.

[1] A. J. Scroggie, W. J. Firth, G. S. McDonald, M. Tlidi, R. Lefever, and L. A. Lugiato, Chaos, Solitons Fractals **4**, 1323 (1994).

[2] F. Leo, S. Coen, P. Kockaert, S.-P. Gorza, P. Emplit, and M. Haelterman, Nat. Photonics **4**, 471 (2010).

[3] A. Roy, R. Haldar, and S. K. Varshney, J. Lightwave Technol. **36**, 5807 (2018).

[4] Y. V. Kartashov, O. Alexander, and D. V. Skryabin, Opt. Express **25**, 11550 (2017).

[5] A. B. Matsko, W. Liang, A. A. Savchenkov, D. Eliyahu, and L. Maleki, Opt. Lett. **41**, 2907 (2016).

[6] H. Taheri, A. A. Eftekhar, K. Wiesenfeld, and A. Adibi, IEEE Photonics J. **7**, 2200309 (2015).

[7] A. Coillet, I. Balakireva, R. Henriet, K. Saleh, L. Larger, J. M. Dudley, C. R. Menyuk, and Y. K. Chembo, IEEE Photonics J. **5**, 6100409 (2013).

[8] S. Coen and M. Erkintalo, Opt. Lett. **38**, 1790 (2013).

[9] Q. Li, T. C. Briles, D. A. Westly, T. E. Drake, J. R. Stone, B. R. Ilic, S. A. Diddams, S. B. Papp, and K. Srinivasan, Optica **4**, 193 (2017).

[10] M. Saha, S. Roy, and S. K. Varshney, Phys. Rev. E **100**, 022201 (2019).

[11] T. Hansson and S. Wabnitz, J. Opt. Soc. Am. B **32**, 1259 (2015).

[12] A. B. Matsko, A. A. Savchenkov, W. Liang, V. S. Ilchenko, D. Seidel, and L. Maleki, Opt. Lett. **36**, 2845 (2011).

[13] L. Zhang, C. Bao, V. Singh, J. Mu, C. Yang, A. M. Agarwal, L. C. Kimerling, and J. Michel, Opt. Lett. **38**, 5122 (2013).

[14] X. Guo, C.-L. Zou, H. Jung, Z. Gong, A. Bruch, L. Jiang, and H. X. Tang, Phys. Rev. Appl. **10**, 014012 (2018).

[15] E. S. Lamb, D. R. Carlson, D. D. Hickstein, J. R. Stone, S. A. Diddams, and S. B. Papp, Phys. Rev. Appl. **9**, 024030 (2018).

[16] L. A. Lugiato and R. Lefever, Phys. Rev. Lett. **58**, 2209 (1987).

[17] R. Haldar, A. Roy, P. Mondal, V. Mishra, and S. K. Varshney, Phys. Rev. A **99**, 033848 (2019).

[18] P. Grelu, *Nonlinear Optical Cavity Dynamics: From Microresonators to Fiber Lasers*, 1st ed. (Wiley-VCH, Wienheim, 2016).

[19] C. Joshi, A. Klenner, Y. Okawachi, M. Yu, K. Luke, X. Ji, M. Lipson, and A. L. Gaeta, Opt. Lett. **43**, 547 (2018).

[20] S. Fujii, A. Hori, T. Kato, R. Suzuki, Y. Okabe, W. Yoshiki, A.-C. Jinnai, and T. Tanabe, Opt. Express **25**, 28969 (2017).

[21] G. DâAguanno and C. R. Menyuk, Eur. Phys. J. D **71**, 1 (2017).

[22] J.-W. Ryu, S.-Y. Lee, and S. W. Kim, Phys. Rev. A **79**, 053858 (2009).

[23] R. Suzuki, S. Fujii, A. Hori, and T. Tanabe, IEEE Photonics J. **11**, 6100511 (2019).

[24] E. Averlant, M. Tlidi, K. Panajotov, and L. Weicker, Opt. Lett. **42**, 2750 (2017).

[25] A. U. Nielsen, B. Garbin, S. Coen, S. G. Murdoch, and M. Erkintalo, Phys. Rev. Lett. **123**, 013902 (2019).

[26] K. Luo, J. K. Jang, S. Coen, S. G. Murdoch, and M. Erkintalo, Opt. Lett. **40**, 3735 (2015).

[27] J. K. Jang, M. Erkintalo, S. Coen, and S. G. Murdoch, Nat. Commun. **6**, 7370 (2015).

[28] E. Lucas, G. Lihachev, R. Bouchand, N. G. Pavlov, A. S. Raja, M. Karpov, M. L. Gorodetsky, and T. J. Kippenberg, Nat. Photonics **12**, 699 (2018).

[29] M. Anderson, Y. Wang, F. Leo, S. Coen, M. Erkintalo, and S. G. Murdoch, Phys. Rev. X **7**, 031031 (2017).

[30] X. X. Jin, Z. C. Wu, L. Li, Q. Zhang, D. Y. Tang, D. Y. Shen, S. N. Fu, D. M. Liu, and L. M. Zhao, IEEE Photonics J. **8**, 1501206 (2016).

[31] Y. Luo, J. Cheng, B. Liu, Q. Sun, L. Li, S. Fu, D. Tang, L. Zhao, and D. Liu, Sci. Rep. **7**, 2369 (2017).

[32] Y. Du, X. Shu, and P. Chengu, Opt. Express **25**, 1131 (2017).

[33] S. T. Cundiff, B. C. Collings, and K. Bergman, Chaos **10**, 613 (2000).

[34] V. Tsatourian, S. V. Sergeyev, C. Mou, A. Rozhin, V. Mikhailov, B. Rabin, P. S. Westbrook, and S. K. Turitsyn, Sci. Rep. **3**, 3154 (2013).

[35] G. P. Agrawal, *Nonlinear Fiber Optics*, 5th ed. (Academic Press, New York, 2013).

[36] M. Haelterman, S. Trillo, and S. Wabnitz, J. Opt. Soc. Am. B **11**, 446 (1994).

[37] R. A. Chipman, W.-S. T. Lam, and G. Young, *Polarized Light and Optical Systems*, 2nd ed. (CRC Press, Boca Raton, 2018).

[38] P. Balla and G. P. Agrawal, Phys. Rev. A **98**, 023822 (2018).

[39] T. Hansson, M. Bernard, and S. Wabnitz, J. Opt. Soc. Am. B **35**, 835 (2018).